EES Catalysis

Accepted Manuscript

This article can be cited before page numbers have been issued, to do this please use: J. Wang, X. Yu, Y. Sun, Y. Zang, X. Yu, H. Tao, C. Lian and H. Qiu, *EES Catal.*, 2026, DOI: 10.1039/D6EY00096G.

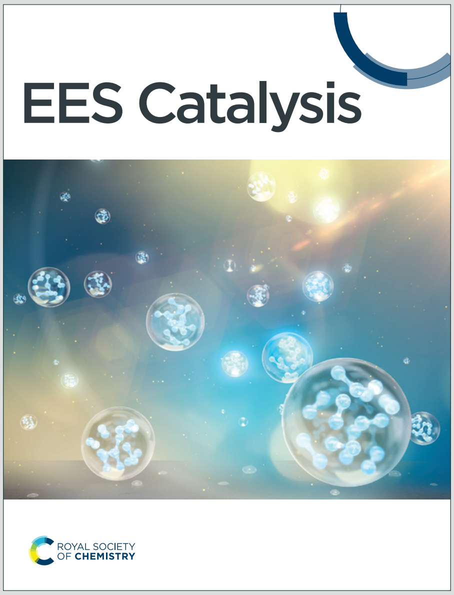

ROYAL SOCIETY
OF **CHEMISTRY**

View Article Online
DOI: 10.1039/D6EY00096G

Broader Context Statement

Electrochemical reconstruction of amorphous metallic materials presents an exceptional opportunity for catalyst design. However, the transformation into highly active metastable crystalline phases with unique electronic structures is rarely discovered. Here, we develop a micellar film-mediated strategy to facilely fabricate large-area mesoporous films of amorphous Ru-W bimetallic composite, involving hierarchical "pyridyl–Ru^{3+}–WS_4^{2-}" coordination and crystallization-retarding pyrolysis. Notably, the amorphous Ru-W bimetallic sulfide exhibits an unconventional reconfiguration from amorphous to crystalline-1T-phase during the electrochemical hydrogen evolution reaction. Theoretical calculations reveal that this transformation originates from electrochemical injection of electrons, which induces interatomic charge redistribution to establish a new coordination environment, thereby driving the atomic rearrangement. In this process, the bridged sulfur provides a critical and efficient synergistic charge transfer pathway that simultaneously ensures the structural stability of the 1T-phase. Taking advantage of the persistent electrochemical reorganization into the highly active 1T-phase, such amorphous catalyst exhibits outstanding long-term stability and superior electrocatalytic activity for hydrogen evolution. In general, the open and coordinative soft environment of the micellar film provides an innovative platform for the tunable synthesis of functional amorphous composites and the subsequent phase engineering toward highly active electrocatalysts for sustainable energy conversion technologies.

View Article Online
DOI: 10.1039/D6EY00096G

ARTICLE

Electrochemical amorphous-to-1T-phase reconfiguration of Ru-W bimetallic sulfide for sustainable hydrogen evolution

Received 00th January 20xx,
Accepted 00th January 20xx

DOI: 10.1039/x0xx00000x

Jingchun Wang[a‡], Xiao Yu[b‡], Yan Sun[a*], Yipeng Zang[c], Xujiang Yu[d], Haolan Tao[b*], Cheng Lian[b*], Huibin Qiu[a*]

Electrochemical reconfiguration of amorphous metallic materials offers exceptional opportunities for catalyst design. Here, we demonstrate a distinctive reconfiguration route toward highly active crystalline 1T-phase in amorphous Ru-W bimetallic sulfide. A micellar film-mediated strategy is developed to facilely fabricate large-area mesoporous films of the amorphous composite, involving sequential accumulation and association of Ru^{3+} and WS_4^{2-} precursors through hierarchical "pyridyl–Ru^{3+}–WS_4^{2-}" coordination, followed by crystallization-retarding pyrolysis. The resulting catalyst reveals appealing hydrogen evolution performance, with a low initial overpotential of 11 mV at 10 mA cm^{-2} and high sustainability at 1.0 A cm^{-2} over 1600 h. Notably, sustained electrochemical stimuli triggers an distinctive amorphous-to-crystalline reconfiguration, gradually generating crystalline Ru-W bimetallic sulfide with a metastable 1T-phase. This substantially endows the catalyst with a remarkable long-term stability while further enhancing the catalytic activity (overpotential of merely 4 mV at 10 mA cm^{-2}). Theoretical calculations reveal a electrochemical-dependent structural reorganization process, where external electron injection triggers charge redistribution that drives the atomic rearrangement, while the sulfur-bridged structure promotes efficient cooperative charge transfer and ensures the structural robustness of the metastable 1T-phase during the reconfiguration.

Introduction

Amorphous metallic materials inherently possess high-density structural defects, unsaturated coordination sites, and tunable local bonding environments[1-6]. Such features effectively reduce the reaction energy barrier and optimize the mass transport pathways, leading to frontier catalytic systems for critical electrochemical reactions, including hydrogen evolution and carbon dioxide reductions[7-14]. Notably, the metastable characteristics render them highly susceptible to dynamic structural evolution under electrochemical conditions, presenting both opportunities for performance modulation and challenges for mechanistic understanding of electrochemical reconfiguration[15, 16]. Utilizing this evolution to rationally generate active species has emerged as a critical strategy to construct efficient and stable catalytic systems[17-20]. To date, the reconfiguration of amorphous materials predominantly yields amorphous-to-amorphous transitions, occasionally accompanied by nanoscale surface/local crystallization/passivation or phase separation induced by elemental leaching[21-28] (Fig. 1a). The resulting crystalline products (e.g., metals, oxides, or hydroxides[29-33], etc.) are typically thermodynamically stable, while metastable phases with special electronic structures and high activity are rarely discovered.

Metal sulfides (e.g., WS_2, MoS_2, etc.) with unique/tunable electronic structure and abundant active sites create favorable conditions for various catalytic processes[34-38]. Particularly, the thermodynamically metastable 1T-phase exhibits exceptional electrochemical activity due to its metallic conductivity, octahedral coordination, and extensible interlayer spacing that facilitates charge transfer[39]. It can be controllably prepared with various approaches, including direct synthesis (e.g., ion intercalation, chemical vapor deposition, etc.)[40-44] and external field-controlled transformations (e.g., strain, plasma induction, etc.)[45-49]. However, the generation of 1T-phase by direct electrochemical reconfiguration from amorphous materials remains unexplored. The amorphous metal sulfides prepared by current methods (e.g., wet-chemical method, chemical vapor deposition)[50-52] have not yet been employed as the critical precursors for the electrochemical reconfiguration to generate 1T-phase.

---

[a] State Key Laboratory of Synergistic Chem-Bio Synthesis, School of Chemistry and Chemical Engineering, Frontiers Science Center for Transformative Molecules, State Key Laboratory of Micro-Nano Engineering Science, Shanghai Jiao Tong University, Shanghai 200240, China
[b] State Key Laboratory of Chemical Engineering and Low-Carbon Technology, School of Chemistry and Molecular Engineering, East China University of Science and Technology, Shanghai 200237, China
[c] State Key Laboratory of Catalysis, Dalian Institute of Chemical Physics, Chinese Academy of Sciences, Dalian 116023, China.
[d] State Key Laboratory of Metal Matrix Composites, School of Materials Science and Engineering, Zhangjiang Institute for Advanced Study, Shanghai Jiao Tong University, Shanghai 200240, China
‡J. Wang and X. Yu contributed equally to this work.
*Email: syzzyy07@sjtu.edu.cn; haolan_tao@ecust.edu.cn; liancheng@ecust.edu.cn; hbqiu@sjtu.edu.cn
† Electronic supplementary information (ESI) available. See DOI: 10.1039/x0xx00000x

View Article Online
DOI: 10.1039/D6EY00096G

Herein, we develop a polystyrene-*b*-poly(2-vinylpyridine) (PS-*b*-P2VP) block copolymer micellar film system to mediate the uniform construction of amorphous mesoporous bimetallic sulfide film (Fig. 1b). Specifically, the micellar film enables the sequential accumulation of Ru^{3+} and WS_4^{2-} ions through a hierarchical "pyridyl–Ru^{3+}–WS_4^{2-}" coordination route. Subsequently, in-situ confined pyrolysis of such metal species-accumulated micellar film directly induces the formation of amorphous Ru-W bimetallic sulfide (denoted as RuWS). In particular, the micellar film mitigates excessive co-precipitation of metal species and retards the crystallization kinetics induced by high temperatures, ensuring the preservation of amorphous structures with sulfur-bridged coordination configuration. Notably, during the electrocatalytic reaction, the amorphous film gradually transforms to crystalline Ru-W bimetallic sulfide with a metastable 1T-phase (Fig. 1b). Theoretical calculations further demonstrate that the electrochemical injection of electrons triggers the amorphous-to-crystalline reconfiguration, where the sulfur-bridged structure effectively balances the electron redistribution between various atoms through rapid charge transfer and efficiently handles the structural strain to sustain the metastable crystalline phase.

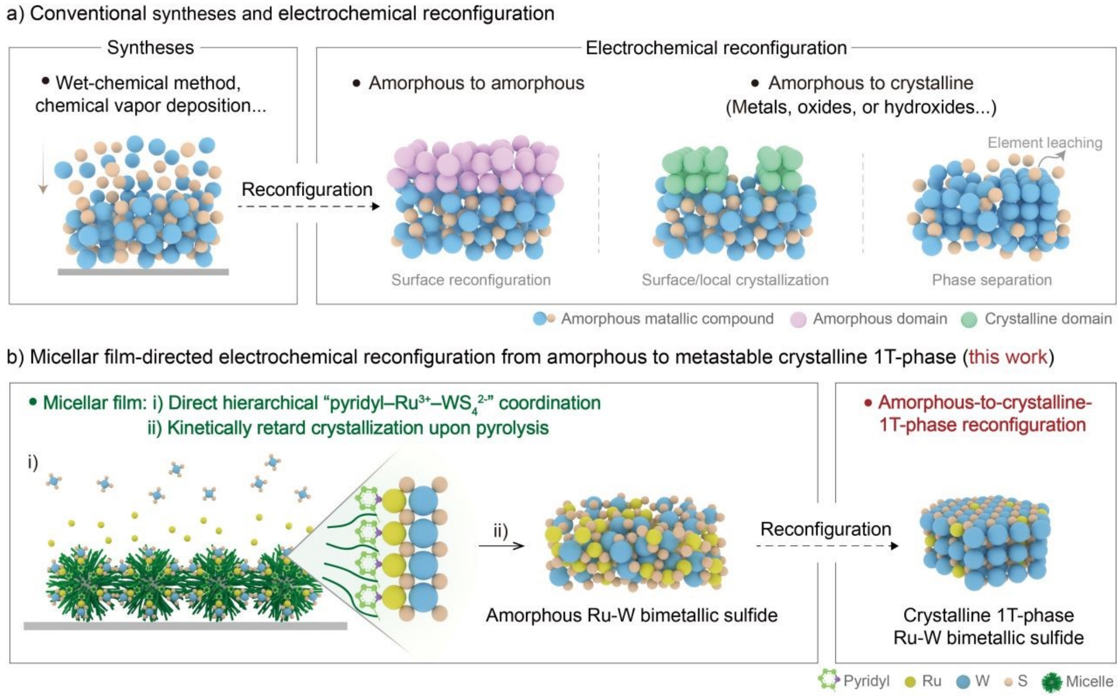

Fig.1 Electrochemical reconfiguration. (a) Traditional syntheses and electrochemical reconfiguration of amorphous materials. (b) Micellar film-mediated formation of amorphous bimetallic sulfide via hierarchical coordination and electrochemical conversion into crystalline bimetallic sulfide with a metastable 1T-phase.

Results and discussion

Fabrication of RuWS-accumulated PS-*b*-P2VP micellar film

Micellar films were prepared on desired substrates via direct drop-casting and rapid solvent evaporation of a solution of PS-*b*-P2VP unimers[53] (Fig. 2a). Such micellar film was solely consisted of a large number of tightly stacked spherical micelles (with a PS core and a P2VP corona) (Fig. S1). Upon treatment in a KOH solution, the micellar film can be separated from the substrate to form a large-area free-standing film (Fig. S2), implying its integral structure and remarkable mechanical robustness. Subsequently, the micellar film was immersed in a solution of $RuCl_3$ in ethanol. While the morphology remained nearly intact, the color of the micellar film gradually became yellow (Fig. 2b), indicating the capture of Ru^{3+} in the P2VP corona of the spherical micelles (Fig. S3), majorly through coordination. Further, upon immersing the Ru^{3+}-loaded micellar film into a solution of $(NH_4)_2WS_4$ in a mixture of 1 : 1 (v/v) isopropanol and water, a brown film was obtained (Fig. 2b). Scanning electron microscopy (SEM) and transmission electron microscopy (TEM) images showed that after the sequentially loading of Ru^{3+} and WS_4^{2-} the micellar film preserved the homogeneous morphology and the internal dense stacking of spherical micelles (Figs. 2c, S4a and S4b). High-resolution TEM (HRTEM) images and fast Fourier transform (FFT) pattern (Figs. S4c and S4d) both demonstrated the absence of crystalline component, which is consistent with the results of X-ray diffraction (XRD) (Fig. S5). High-angle annular dark field scanning transmission electron microscopy (HAADF-STEM) images and elemental mapping further confirmed the relatively homogenous distribution of Ru, W, and S elements (Fig. S4e).

To elucidate the association patterns among pyridyl groups on P2VP, Ru^{3+} and WS_4^{2-}, a factorial cross-comparison analysis was systematically conducted. Fourier transform infrared spectroscopy (FT-IR) spectra showed that while the micellar film barely associated with the $WS4^{2-}$ ions, it reveals a remarkable

View Article Online
DOI: 10.1039/D6EY00026G

association with the Ru^{3+} ions, majorly involving coordination interactions with the pyridyl groups (Fig. 2d). Notably, after the secondary addition of WS_4^{2-} ions, the micellar film revealed attenuated signals for the coordinated pyridyl groups, while the peaks for the free pyridyl groups recovered. It appeared that the introduction of WS_4^{2-} ions triggered a slight dissociation of Ru^{3+} with the pyridyl groups. On the other hand, the direct mixing of Ru^{3+} and WS_4^{2-} in absence of micellar film yielded irregular non-mesostructured RuWS powder (Fig. S6) and UV-vis absorption spectra showed a strong interaction between Ru^{3+} and WS_4^{2-} (Fig. S7). Apparently, the sequential accumulation of Ru^{3+} and WS_4^{2-} ions facilitated a hierarchical coordination of "pyridyl–Ru^{3+}–WS_4^{2-}" (Fig. 2e) in the micellar film, where S bridge the pyridyl groups, Ru^{3+} and WS_4^{2-}. X-ray photoelectron spectroscopy (XPS) spectra of Ru 3p, W 4f and S 2p revealed valence states of Ru at +3, W at +6, and S at -2, respectively, the same as the $RuCl_3$ and $(NH_4)_2WS_4$ precursors (Fig. S8).

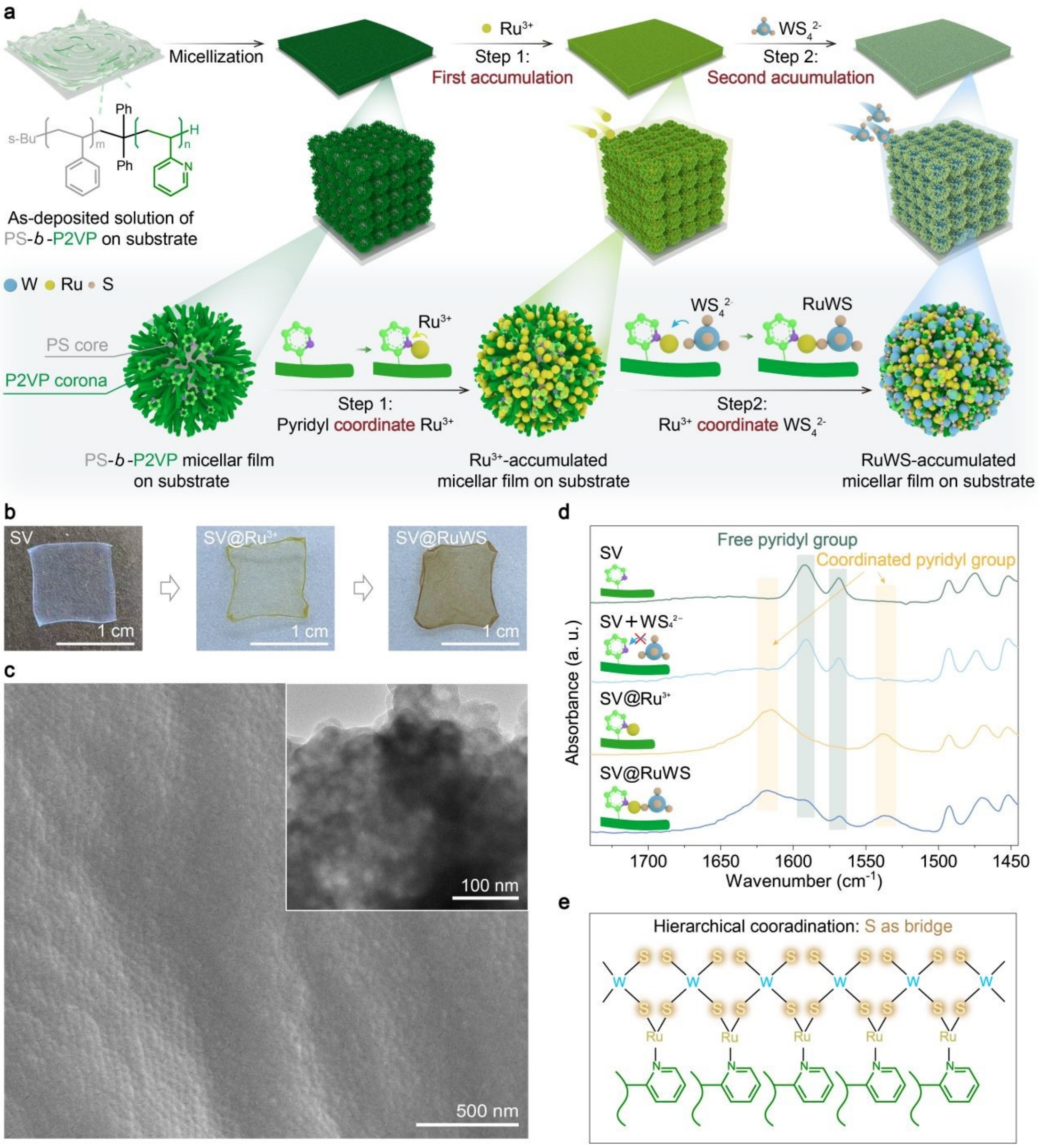

Fig.2 Micellar film-directed sequential accumulation of Ru^{3+} and WS_4^{2-} via hierarchical coordination. (a) Schematic illustration of the preparation of Ru-W bimetallic sulfide-accumulated PS-*b*-P2VP micellar film. (b) Photographs of a free-standing micellar film and that after accumulation of Ru^{3+} ions (denoted as SV@Ru^{3+}) and successive accumulation of both Ru^{3+} and WS_4^{2-} ions (denoted as SV@RuWS). (c) SEM and TEM (inset) images of RuWS-accumulated micellar film. (d) FT-IR spectra of PS-*b*-P2VP micellar film, PS-*b*-P2VP micellar film after immersing in a solution of WS_4^{2-} ions in ethanol, Ru^{3+} ion-accumulated PS-*b*-P2VP micellar film, and RuWS-accumulated PS-*b*-P2VP micellar film (denoted as SV, SV+WS_4^{2-}, SV@Ru^{3+}, and SV@RuWS, respectively). (e) Schematic illustration of the hierarchical coordination.

Fabrication of amorphous mesoporous bimetallic sulfide film

View Article Online
DOI: 10.1039/D6EY00096C

The RuWS-accumulated PS-*b*-P2VP micellar film on a specific substrate was subjected to pyrolysis under nitrogen at 600 ℃ to remove the micellar scaffold (Fig. 3a). This immediately generated a mesoporous film featuring a large-scale integration of uniformly sized spherical cavities and a homogeneous porous surface (Figs. 3b and S9). TEM images showed that the resulting film possessed well-defined mesopores with an average diameter of ca. 28.1 nm (Figs. 3b and S10). In particular, the hierarchical coordination structures provided critical rigid support and constraint for the mesopores[53]. Nitrogen sorption measurements further confirmed such mesoporous structure (Fig. S11). HRTEM, aberration-corrected high-angle annular dark-field scanning transmission electron microscopy (AC-HAADF-STEM) and corresponding fast FFT images (Figs. 3c, S12, and S13) showed that the mesoporous film generally possessed an amorphous framework, with randomly arranged atoms. XRD pattern also demonstrated the amorphous nature (Fig. S14). On the other hand, HAADF-STEM and element mapping images confirmed the co-existence of Ru, W, and S elements and revealed their uniformly distribution throughout the film (Fig. 3d). Additionally, trace carbon and nitrogen residues were presented in this film (Fig. S15). X-ray absorption near-edge structure (XANES) spectra at Ru *K*-edge revealed slightly lower absorption edges for the pyrolyzed sample (Fig. S16a). Meanwhile, the intensity of white line at W L_3-edge in XANES spectra was decreased (Fig. S16b). Such results suggested the lower valence states for both Ru and W,[54, 55] aligning well with the corresponding XPS results (Fig. S17). The corresponding Fourier-transformed extended X-ray absorption fine structure (EXAFS) spectra at W L_3-edge and Ru *K*-edge revealed characteristic peaks at 1.30 and 1.71 Å for W–S and Ru–S coordination, respectively (Figs. 3e and 3f). Notably, no significant correlation signal was observed between the metal atoms. It appeared that the sulfur atoms bridged the Ru and W atoms and facilitates the generation of the amorphous mesoporous RuWS film. This was consistent with the coordination structure of "pyridyl–Ru^{3+}–WS_4^{2-}" in the precursor.

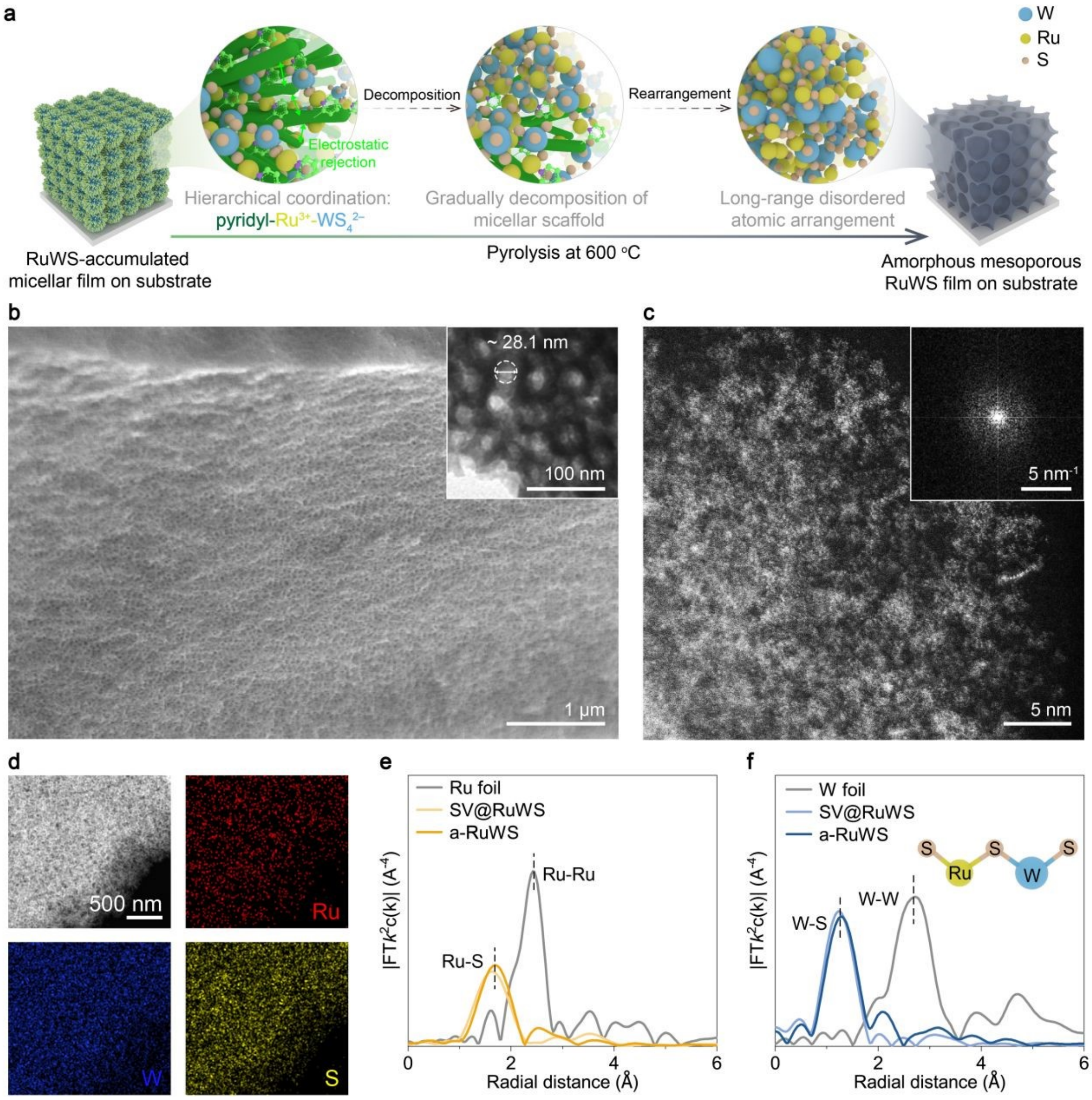

Fig.3 Micellar film-directed formation of amorphous mesoporous RuWS film. (a) Schematic illustration of the conversion of RuWS-accumulated PS-b-P2VP micellar film into mesoporous film of amorphous RuWS upon pyrolysis at 600 °C. (b) SEM and TEM (inset)

View Article Online
DOI: 10.1039/D6EY00006G

images, (c) AC-HAADF-STEM and corresponding FFT with characteristic weak diffusion ring (inset) images, and (d) HAADF-STEM and elemental mapping images of amorphous mesoporous RuWS film. (e, f) EXAFS spectra at (e) Ru *K*-dege and (f) W L_3-edge of amorphous mesoporous RuWS film and RuWS-accumulated micellar film (denoted as a-RuWS and SV@RuWS).

To gain deep insights, the evolution of non-mesostructured RuWS powder and RuWS-accumulated micellar film in the pyrolysis process performed at gradually increasing temperatures were carefully examined (Figs. S18–S31). For non-mesostructured RuWS powder, crystalline domains began to appear upon pyrolysis at 400 °C and dominated at higher temperatures (Figs. S18–S22). The highly crystalline powder formed at 600 °C was solely consisted by isolated Ru and WS_2 phases (Fig. S22). On the contrary, for RuWS-accumulated micellar film, the amorphous mesoporous architecture retained well even after pyrolysis at 600 °C (Figs. 3 and S23–S27), before the generation of homogeneously distributed tiny crystalline nanoparticles at 700 °C and larger crystalline domains at higher temperatures (Figs. S28–S31). It can be anticipated that the spatially confined coordination in the micellar film reduced the collision of Ru, W, and S species, consequently retarding the crystal growth rate within a defined thermal regime. Similarly, the treatment of Mo-based materials yielded mesoporous amorphous Ru-Mo bimetallic sulfide (denoted as RuMoS) film (Fig. S32).

Electrocatalytic performance of amorphous mesoporous RuWS film

Subsequently, the hydrogen evolution reaction (HER) activity of amorphous mesoporous RuWS film on carbon cloth was evaluated using a typical three-electrode system in 1.0 M KOH (Figs. 4 and S33). The amorphous mesoporous RuWS film formed at 600 °C exhibited the optimal performance (Fig. S34) and hence it was predominantly used for further investigation. Commercial Pt/C, crystalline WS_2 powder (derived from pyrolysis of $(NH_4)_2WS_4$ powder at 600 °C, Fig. S35), and crystalline Ru/WS_2 powder (derived from pyrolysis of non-mesostructured RuWS powder at 600 °C) were selected as the control samples. The amorphous mesoporous RuWS film revealed remarkably lower overpotentials of 11 mV at 10 mA cm^{-2} and 48 mV 100 mA cm^{-2} than that of commercial Pt/C (43 and 273 mV), crystalline WS_2 powder (60 and 316 mV) and crystalline Ru/WS_2 powder (26 and 186 mV) (Figs. 4a and S36). In addition, at a high current density of 1000 mA cm^{-2}, the amorphous mesoporous RuWS film also revealed relatively low overpotential of 130 mV and Tafel slope of 23.2 mV dec^{-1} (Figs. 4b and 4c), indicating a superior HER electrocatalytic activity toward industrial applications. Nyquist plots showed that the amorphous mesoporous RuWS film possessed a smaller semicircular diameter in the electrochemical impedance spectroscopy (EIS) compared with other samples, suggesting a lower charge transfer resistance (Figs. S37 and S38). The electrochemical double-layer capacitance (C_{dl}) (134.5 mF cm^{-2}) of amorphous mesoporous RuWS film was significantly higher than that of other samples, implying an increased density of active sites (Figs. 4c and S39). Moreover, the amorphous mesoporous RuWS film also possessed an excellent hydrophilicity that would facilitate the electrocatalytic reaction (Fig. S40). Overall, the self-supported amorphous mesoporous film architecture was more conducive to active site exposure and mass/electron transfer, bringing a considerable improvement of HER activity (Fig. 4d).

Chronoamperometry tests were conducted at current densities of 10, 100 and 1000 mA cm^{-2}, respectively, to evaluate the stability of amorphous mesoporous RuWS film (Figs. 4e and S41). After 100 h of stability testing, negligible current decays with minimal fluctuations were observed at current densities of 10 and 100 mA cm^{-2} (Fig. S41). Notably, the sample displayed a continuous operation at a current density of 1000 mA cm^{-2} for over 1600 h in an alkaline electrolyte with negligible metal leaching confirmed by ICP-OES, demonstrating an exceptional long-term stability (Fig. 4e and Table S1). Surprisingly, the post-test sample revealed even lower overpotential of only 4 mV at 10 mA cm^{-2} and Tafel slope of 10.2 mV dec^{-1} (Figs. 4f and S42), indicating the emergence of obviously enhanced catalytic activity and kinetics. EIS showed that the post-test sample also possessed a decreased charge transfer resistance and thus a more efficient electron transfer capability (Fig. 4g). These features were extremely appealing compared with previously reported amorphous/Ru-based electrocatalysts in alkaline media (Fig. 4h and Table S2). Anion-exchange membrane water electrolyzer (AEMWEs) was assembled using the amorphous mesoporous RuWS film as the cathode and commercial IrO_2 as the anode to further evaluate the practical application potential (Fig. S43a). The assembled AEMWE exhibited a low cell voltage of 1.60 V at a current density of 1.0 A cm^{-2}, and showed no obvious performance degradation during continuous operation for 27 h, confirming favorable potential for practical water electrolysis (Fig. S43b, c).

Electrochemical reconfiguration of amorphous mesoporous RuWS film

To unravel the mechanistic origin of the long-term stability and performance enhancement of amorphous mesoporous RuWS film, we systematically monitored the dynamic evolution of the atomic/electronic structure under the applied negative electric field (Fig. 5a). Uniformly distributed sub-nanometer clusters emerged on the mesoporous film and gradually evolving into nanoparticles (Fig. S44). AC-HAADF-STEM image revealed the expanding of crystalline domains in the amorphous matrix and the eventual formation of large-area crystalline phases. The resulting crystalline region showed distinct wide lattice stripes (0.677 nm) corresponding to WS_2 (Fig. S45) and clear tetragonal lattice arrangements for 1T-phase (Figs. 5b and 5c). The intensity distribution map of the blue lines specifically revealed two sulfur atoms between the neighboring tungsten atoms, indicating an octahedral coordinated 1T-phase atomic pattern[42] (W–S–S–W, Figs. 5c and 5e). Notably, a considerable number of atomic-level dark spots were detected on the WS_2 crystal (Fig. 5d, marked with yellow circles), which could be ascribed to the doping of Ru atoms. The corresponding HAADF intensity line profiles further confirmed the existence of Ru single atoms (Figs. 5e and S46). XANES spectrum at Ru *K*-edge showed slightly higher absorption edge for the post-test sample, indicating an increased oxidation state of Ru element (Fig. S47). EXAFS spectra exhibited a prominent peak at 1.52 Å corresponding to the Ru–S scattering feature and thus confirmed the isolated dispersion of Ru atoms (Fig. 5f). Compared with 2H-phase WS_2, the characteristic (002) peak of the reconstructed 1T-phase exhibited a distinct negative shift, indicating the introduction of Ru increased the interlayer spacing[49] (Fig. S48). The positively shifted Ru 3p signal of XPS further indicated an elevated valence state of Ru (Fig. S49a). Meanwhile, the negative shift of the S 2p signals implied that the Ru atoms probably possessed a positive valence state via the association with S atoms in the WS_2 matrix (Fig. S49b).

In addition, Raman spectroscopy revealed progressively intensified peaks of 1T WS_2 at 138, 212, 286, and 350 cm^{-1} with increasing testing time, indicating a growing fraction of the 1T-phase[42, 49] (Fig. 5g). The W 4f of XPS spectrum exhibited two new peaks at 31.7 and 33.9 eV after test, approximately 0.9 eV lower than the corresponding peaks in 2H WS_2, which can be assigned to the formation of 1T WS_2[37] (Figs. 5h and S35e). Accordingly, the content of converted 1T-phase estimated from integrated peak areas reached 82.7% at 120 h (Table S3). Meanwhile, the EXAFS spectra evolved as a function of time, featuring the emergence and intensification of a new peak, attributing to W–W coordination (Fig. 5i). The concomitant elongation of both W–S and W–W bonds to 2.04 and 2.87 Å, respectively, was consistent with the structural characteristics of the 1T WS_2[37, 56, 57], further implying the atomic reconstruction during the electrocatalytic test (Figs. 5i, S50–S53 and Table S4)

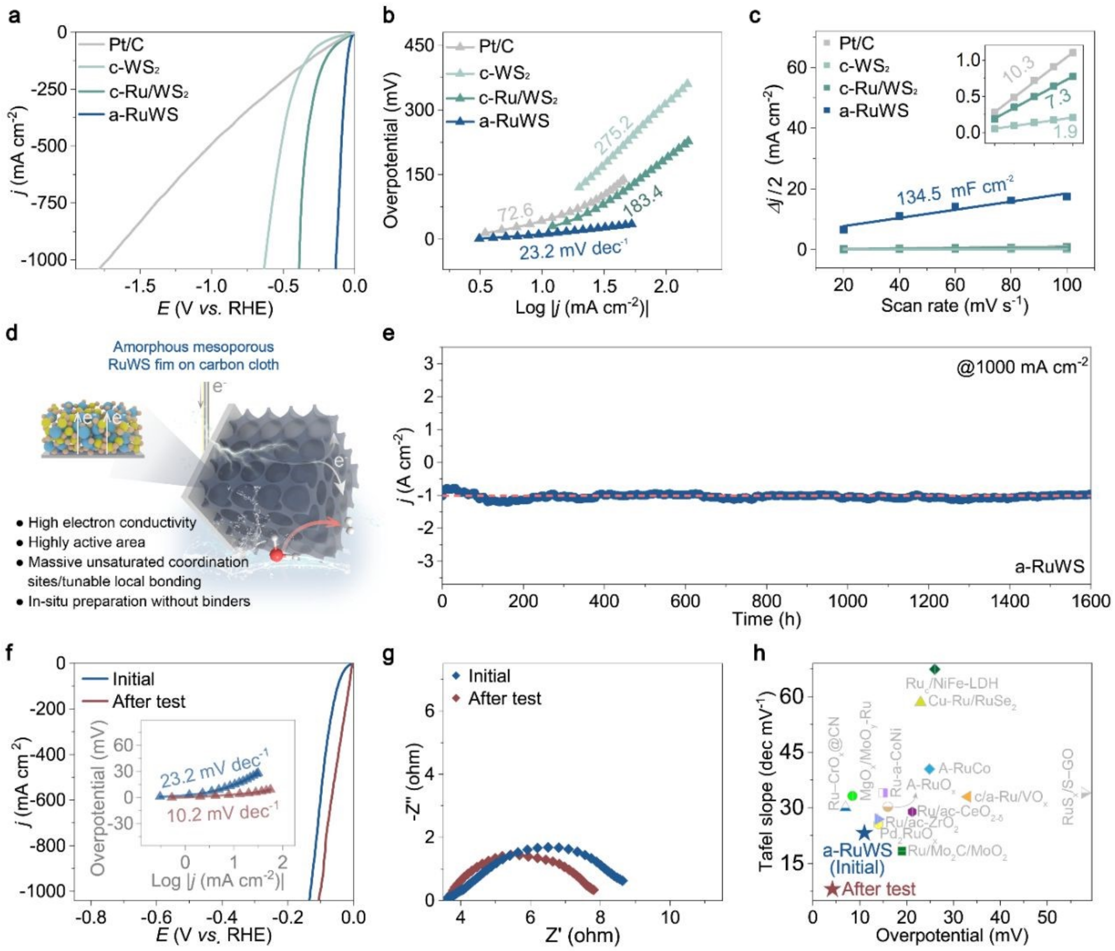

Fig.4 Electrocatalytic performance of amorphous mesoporous RuWS film. (a) HER linear sweep voltammetry (LSV) curves with *iR*-correction, (b) Tafel slopes for HER, and (c) plots of current density versus scan rate of commercial Pt/C, crystalline WS_2 (denoted as c-WS_2), crystalline WS_2 with Ru nanoparticles (denoted as c-Ru/WS_2), and amorphous mesoporous RuWS film (denoted as a-RuWS) in an aqueous solution of 1.0 M KOH. (d) Schematic illustration of the advantageous catalytic environment of amorphous mesoporous RuWS film on carbon cloth. (e) Chronoamperometry curves of amorphous mesoporous RuWS film at 1000 mA cm^{-2}. (f) LSV curves and Tafel slopes (inset), and (g) EIS Nyquist plots of amorphous mesoporous RuWS film before and after the HER stability test. (h) Comparison of overpotential and Tafel slope with other reported amorphous/Ru-based HER electrocatalysts.

Mechanism for electrochemical amorphous-to-crystalline-1T-phase reconfiguration

First-principles calculations were performed to elucidate the atomic-level mechanism for the electrochemically induced reconfiguration[56, 58, 59] (Fig. 6). Three structural models of the amorphous Ru-W sulfide phase featuring a sulfur-bridged network of metal atoms with coordination-unsaturated W and S sites, namely amorphous RuWS-1, RuWS-2 and RuWS-3, were

View Article Online
DOI: 10.1039/D5EY00

constructed and geometrically stabilized through structure optimization (Fig. 6a). To reduce the calculation complexity, only one Ru atom was involved in each model. Taking the standard structure of 1T-phase Ru-WS$_2$ as the baseline state, the atomic disorder increases progressively from amorphous RuWS-1 to RuWS-3 with consistent atom number and element species, corresponding to a gradual rise in structural free energy. The energy trend indicates a thermodynamic driving force for the conversion from the disordered amorphous states toward 1T-phase Ru-WS$_2$.

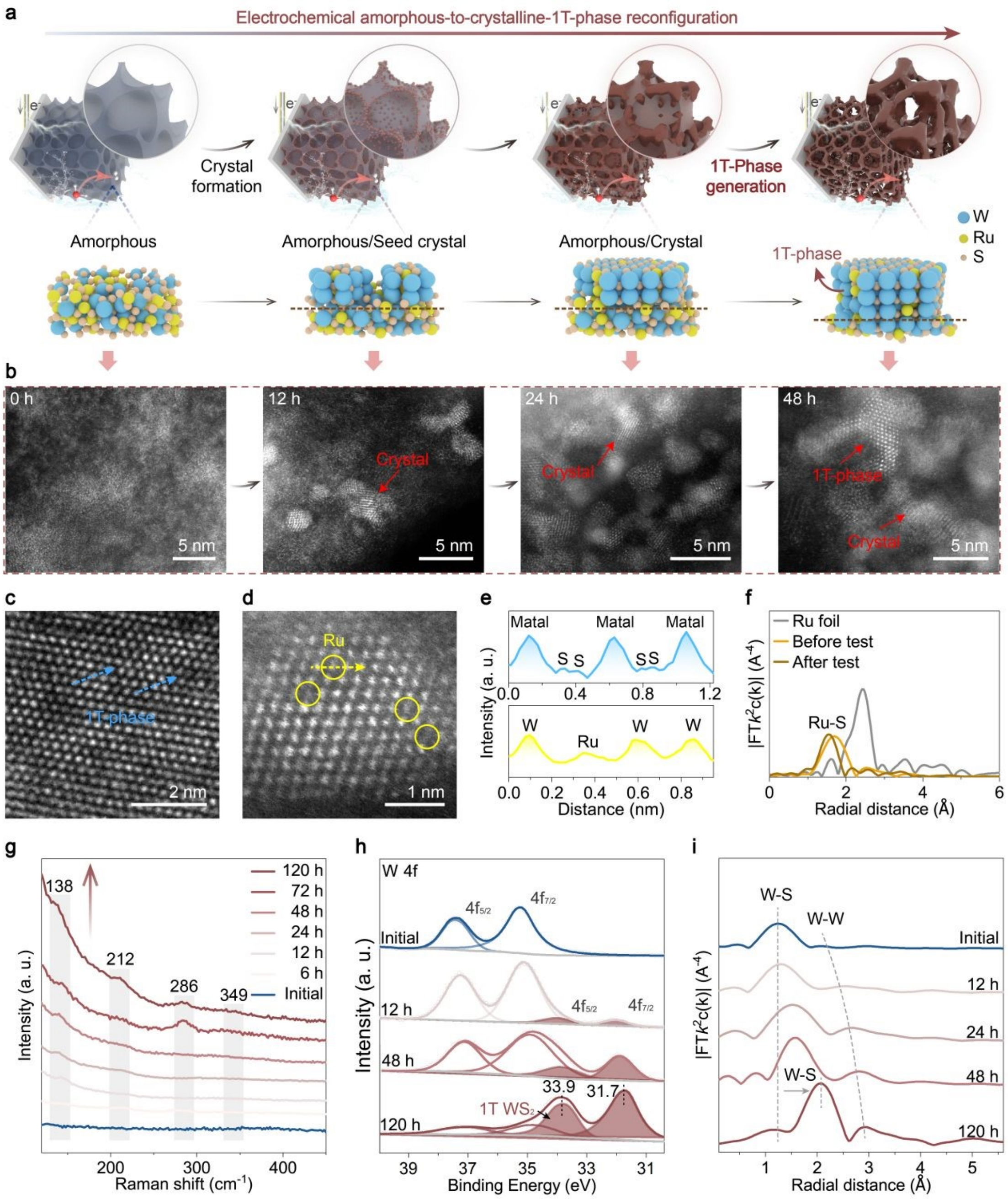

Fig.5 Reconfiguration of amorphous mesoporous RuWS film during the electrochemical process. (a) Schematic illustration of gradual formation of crystalline nuclei from amorphous mesoporous RuWS film during the electrochemical process, followed by the ultimate generation of crystalline Ru-W bimetallic sulfide with 1T-phase. (b) AC-HAADF-STEM images of generation from amorphous mesoporous RuWS film during the electrochemical test. (c) HRTEM and (d) AC-HAADF-STEM images of amorphous mesoporous RuWS film after electrochemical test. (e) Atomic arrangement profiles along the marked lines in (c, d). (f) EXAFS spectra at the Ru *K*-edge of amorphous mesoporous RuWS film before and after the electrochemical test. (g) Raman spectra, (h) high-resolution XPS spectra of W 4f and (i) EXAFS spectra at W L_3-edge of amorphous mesoporous RuWS film at various periods of the electrochemical test.

View Article Online
DOI: 10.1039/D6EY00096G

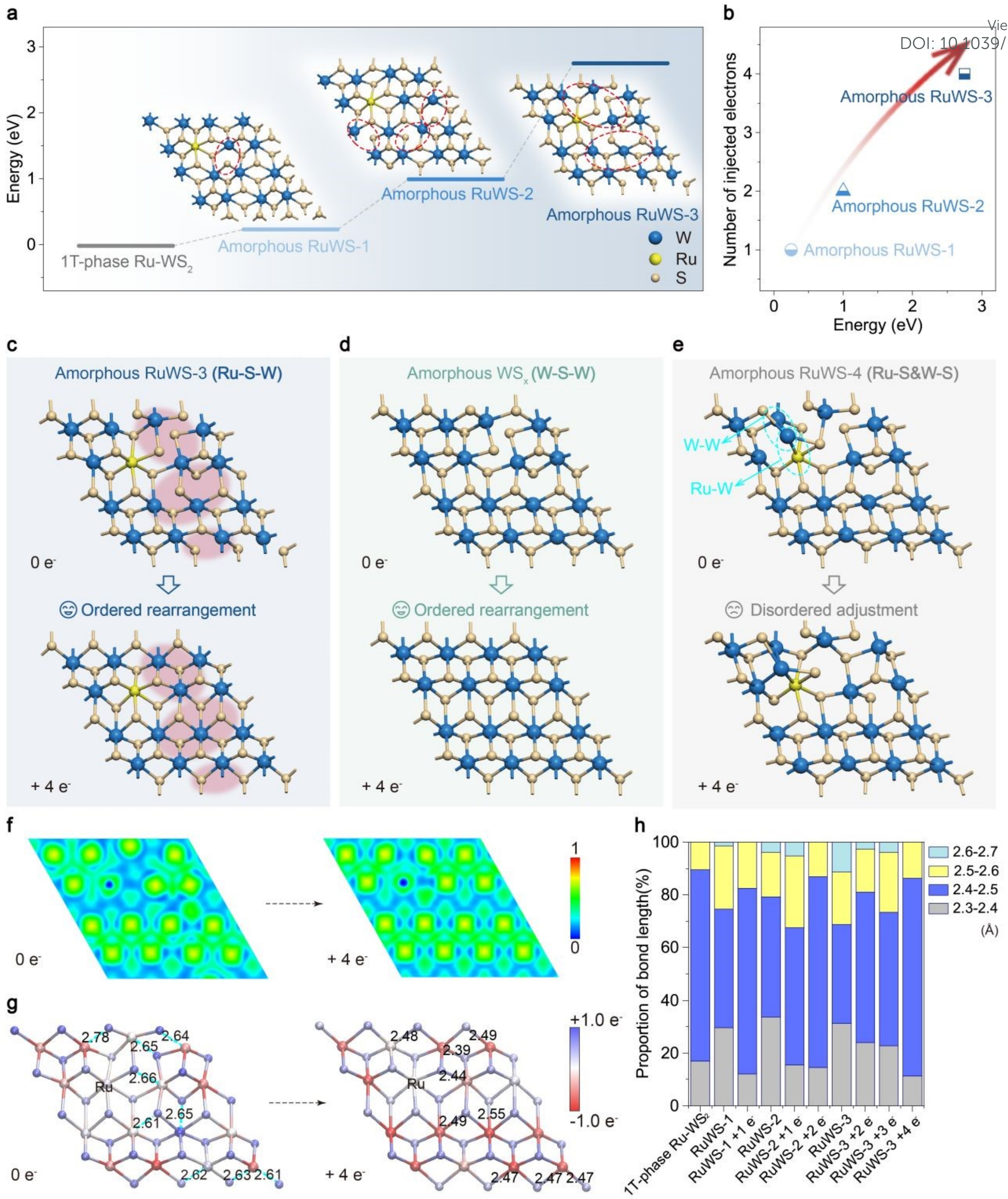

Fig.6 Mechanism investigation on electrochemical amorphous-to-crystalline reconfiguration. (a) Free energies of three disordered configurations of amorphous Ru-W bimetallic composites with increasing atomic disorder, referenced to the standard 1T-phase Ru-WS$_2$ as the baseline state. (b) Number of injected electrons required for the reconfiguration. (c–e) Atomic configurations of (c) amorphous RuWS-3, (d) amorphous WS$_x$, and (e) amorphous RuWS-4 before and after being injected with 4 electrons. (f) Variation of electron localization function before and after being injected with 4 electrons in amorphous RuWS-3. The red and blue areas represent electron localization and delocalization, respectively. (g) Bader charge on amorphous RuWS-3 and relevant bond lengths before and after the injection of 4 electrons. Red represents lost electrons, and blue represents gained electrons. The unit of bond length is angstrom (Å). (h) Proportion of bonds with different lengths in various structures.

However, both theoretical analysis and experimental observation show that the amorphous configurations are locally stable. It implies that the transformation is kinetically hindered, therefore requiring a substantial external driving force to proceed at an appreciable rate. To mimic the electrochemical environment presented in HER, further calculations were performed on the amorphous Ru-W sulfide models with additional electrons to simulate the effect of an applied negative potential. Interestingly, all of these three structures undergo atomic coordination and ordered rearrangement following the electron injection, resulting in the formation of 1T-phase Ru-WS_2 (Figs. 6c and S54). In particular, amorphous RuWS-1 requires only one electron for shifting from a disordered atomic arrangement to an ordered 1T-phase, whereas amorphous RuWS-2 and amorphous RuWS-3 necessitate the addition of two and four electrons, respectively. It is worth noted that the number of external electron injection required for the structural evolution is related with the free energy of the amorphous structures, which intrinsically depends on the degree of atomic disorder (Fig. 6b). This suggests an electrochemically driven mechanism for structural reorganization in the amorphous Ru-W bimetallic sulfide, triggering directional construction of its metastable crystalline phase by satisfying the electronic requirements. This is consistent with the electrocatalytic stability results at different applied potentials.

To further explore the influence of catalyst structure in this reconfiguration, disordered atomic configurations of amorphous WS_x with metal network (denoted as amorphous WS_x) as well as amorphous Ru-W bimetallic sulfide with the presence of Ru-W and W-W bonds (denoted as amorphous RuWS-4) were constructed and fully optimized by selectively replacing Ru and S with W atoms in amorphous RuWS-3, respectively (Figs. 6d, 6e and S55). Notably, after injecting four electrons into each geometrically optimized structure, the former achieved ordered rearrangement to form an atomic configuration of 1T WS_2, while the latter remained in a disordered state. It seems that the establishment of sulfur-bridged metal networks within the disordered structure is crucial for the amorphous to metastable crystalline phase reconfiguration under electrochemical induction. In addition, sulfur-bridged amorphous RuMoS also undergoes atomic rearrangement upon electron injection, further highlighting the critical role of such bridging motifs during the reconstruction (Fig. S56). As visualized in the electron localization functions for the stabilized amorphous RuWS-3 (Fig. 6f), an obvious electron delocalization effect is observed around the structure defects. Accompanying electron injection, external electrons in amorphous RuWS-3 are more localized at the structure defects to promote the reconfiguration, and thus undergoing an ordered rearrangement of the local electron density (Figs. S57–S59). The structural reconfiguration of amorphous WS_x align with the above results, while amorphous RuWS-4 exhibits more serious electron redistribution. It primarily stems from the coexisting metal-metal and metal-sulfide bonds, whose inherent disparity drives irregular transfer of electrons (Figs. S60 and S61).

Furthermore, Bader charges among atoms in amorphous RuWS-1, amorphous RuWS-2, amorphous RuWS-3, and amorphous WS_x all redistribute upon electron injection. These demonstrate that the enhanced interatomic interactions originated from the electron transfer, thereby driving the reconfiguration of these disordered structures into the crystalline 1T-phase (Figs. 6g and S62–S64). The increased electron loss in the metallic atoms and the enhanced electron capture ability of S atoms reveal that the electrons transfer directionally from the metal center to the bridging S atoms (Fig. S62). Such result is consistent with the distinct negative shift of the peak in S 2p XPS spectrum (Fig. S49b). It implies that the electron transfer between metal and S atoms in the disordered structures exhibit a "metal to sulfur" polarity in the bonding. Such enhanced polarization effect promotes the bonding strength of metal-sulfur bonds[57], thereby readily stimulating new bond formation. In the pristine structure, the substantial charge disparity between defect-site S atoms and fully coordinated S atoms is alleviated after electronic injection, leading to a more uniform distribution of electrons on the sulfur atoms (Figs. 6g and S62–S64). In contrast, such equilibration of electron distribution is suppressed in amorphous RuWS-4 due to the presence of metallic Ru-Ru and W-W bonds (Fig. S65). These observations confirm that the bridging effect of sulfur atoms enables the metal network to achieve efficient interatomic cooperative charge redistribution, ensuring the structural stability for metastable crystalline phase during the atomic rearrangement. Statistical analysis of bond length distributions before and after electron injection in amorphous RuWS-1, amorphous RuWS-2 and amorphous RuWS-3 shows that the length distribution of W-S bond in the reconstructed 1T-phase Ru-WS_2 has approximately 70% of bonds falling within the 2.4–2.5 Å range, with no bonds exceeding 2.6 Å. This is extremely similar to the standard 1T-phase Ru-WS_2 structure (Fig. 6h), further confirming the generation of metastable crystalline 1T-phases relying on electrocatalytic structural reconfiguration. Indeed, the Ru-S bond length remains largely unchanged before and after reconfiguration, maintaining an average value of 2.6 Å (Table S5).

Conclusions

In summary, we have employed a micellar film system to prepare large-area mesoporous films of amorphous bimetal sulfide through hierarchical "pyridyl–Ru^{3+}–WS_4^{2-}" coordination and retarded crystallization. Such amorphous materials revealed excellent HER performance and long-term stability. Interestingly, the electrochemical process induced an "amorphous-to-crystalline" transition and eventually generated crystalline Ru-W bimetallic sulfide with a thermodynamically metastable but electrochemically more favored 1T-phase. Theoretical calculations demonstrated that the reconfiguration is triggered by sufficient electron injection, and the sulfur-bridged metallic network creates rapid charge transfer pathways to ensure the stable maintenance of the reconfigured 1T-phase. Notably, the reconfigured catalyst formed after a 1600-h electrochemical test revealed a remarkably reduced overpotential of only 4 mV at a current density of 10 mA cm^{-2}. Overall, this work not only provides an innovative route to functional amorphous composites, especially with a mesoporous film feature, but also establishes a novel paradigm for phase engineering toward highly active electrocatalysts, aiming at advanced sustainable energy conversion technologies.

Author contributions

J.W. designed and conducted the experiments, performed the catalyst preparation, characterization and catalytic tests, analyzed the data and wrote the paper. Y.S. supervised the experiments. X.Y. and H.T. performed the DFT calculations. C.L. and H.Q. supervised the project and revised the paper. All the authors discussed the results and commented on the paper.

Conflicts of interest

There are no conflicts to declare.

Data availability

The data supporting this article have been included as part of the Supplementary Information†.

Acknowledgements

We thank the financial support from the National Natural Science Foundation of China (22425203, 22502117) and the Innovation Program of Shanghai Municipal Education Commission (202101070002E00084). This work was also supported by BL13SSW and the User Experiment Assist System of Shanghai Synchrotron Radiation Facility (SSRF).

Notes and references

1. S. Lan, L. Zhu, Z. Wu, L. Gu, Q. Zhang, H. Kong, J. Liu, R. Song, S. Liu, G. Sha, Y. Wang, Q. Liu, W. Liu, P. Wang, C.-T. Liu, Y. Ren and X.-L. Wang, *Nat. Mater.*, 2021, **20**, 1347-1352.
2. Y. Liu, A. Madanchi, A. S. Anker, L. Simine and V. L. Deringer, *Nat. Rev. Mater.*, 2024, **10**, 228-241.
3. J. Zhang, L. Xu, X. Yang, S. Guo, Y. Zhang, Y. Zhao, G. Wu and G. Li, *Angew. Chem. Int. Ed.*, 2024, **63**, e202405641.
4. C. Pei, S. Chen, T. Zhao, M. Li, Z. Cui, B. Sun, S. Hu, S. Lan, H. Hahn and T. Feng, *Adv. Mater.*, 2022, **34**, 2200850.
5. Z. Su, X. Chen, M. Sun, X. Yang, J. Kang, Z. Cai and L. Guo, *Angew. Chem. Int. Ed.*, 2024, **64**, e202416878.
6. J. Wang, L. Zhao, Y. Zou, J. Dai, Q. Zheng, X. Zou, L. Hu, W. Hou, R. Wang, K. Wang, Y. Shi, G. Zhan, Y. Yao and L. Zhang, *J. Am. Chem. Soc.*, 2024, **146**, 11152-11163.
7. F. Feng, C. Ma, S. Han, X. Ma, C. He, H. Zhang, W. Cao, X. Meng, J. Xia, L. Zhu, Y. Tian, Q. Wang, Q. Yun and Q. Lu, *Angew. Chem. Int. Ed.*, 2024, **63**, e202405173.
8. Y. Mu, D. Zhang, T. Gao, L. Wang, L. Zhang, X. Zou, W. Zheng, J. Fan and X. Cui, *Angew. Chem. Int. Ed.*, 2025, **64**, e202505908.
9. C. Wan, Z. Zhang, J. Dong, M. Xu, H. Pu, D. Baumann, Z. Lin, S. Wang, J. Huang, A. H. Shah, X. Pan, T. Hu, A. N. Alexandrova, Y. Huang and X. Duan, *Nat. Mater.*, 2023, **22**, 1022-1029.
10. E. Shin, D.-H. Kim, M. Sagong, J. Choe, S. H. Park, J. Ahn, J. W. Baek, M. Kim, S. Woo, Y. Cho, S.-J. Choi, S.-J. Kim, J. M. Yuk, J. Li, S.-Y. Choi and I. D. Kim, *Adv. Mater.*, 2025, **37**, 2419790.
11. D. Zhang, F. Wang, W. Zhao, M. Cui, X. Fan, R. Liang, Q. Ou and S. Zhang, *Adv. Sci.*, 2022, **9**, 2202445.
12. Y. Li, Q. Yin, B. Jia, H. Wang, H. Gu, Q. Hu, H. Yang, T. Guo, P. Hu, L. Li, L. M. Liu and L. Guo, *Angew. Chem. Int. Ed.*, 2025, **64**, e202505668.
13. J. A. Bau, A.-H. Emwas, P. Nikolaienko, A. A. Aljarb, V. Tung and M. Rueping, *Nat. Catal.*, 2022, **5**, 397-404.
14. J. Staszak-Jirkovský, Christos D. Malliakas, Pietro P. Lopes, N. Danilovic, Subrahmanyam S. Kota, K.-C. Chang, B. Genorio, D. Strmcnik, Vojislav R. Stamenkovic, M. G. Kanatzidis and N. M. Markovic, *Nat. Mater.*, 2015, **15**, 197-203.
15. W. Ding, D. Ji, K. Wang, Y. Li, Q. Luo, R. Wang, L. Li, X. Qin and S. Peng, *Angew. Chem. Int. Ed.*, 2024, **64**, e202418640.
16. J. Liu and L. Guo, *Matter*, 2021, **4**, 2850-2873.
17. G. Chen, Z. Hu, Y. Zhu, B. Gu, Y. Zhong, H. J. Lin, C. T. Chen, W. Zhou and Z. Shao, *Adv. Mater.*, 2018, **30**, 1804333.
18. Y. Yue, X. Zhong, M. Sun, J. Du, W. Gao, W. Hu, C. Zhao, J. Li, B. Huang, Z. Li and C. Li, *Adv. Mater.*, 2025, 2418058.
19. X.-Y. Zhang, S.-S. Yu, J.-J. Chen, K. Gao, H.-Q. Yu and Y. Yu, *Adv. Mater.*, 2025, **37**, 2419050.
20. M. Liu, H. Su, X. Liu, X. He, P. Tan, F. Liu and J. Pan, *Nat. Commun.*, 2025, **16**, 2826.
21. J. Nie, J. Shi, L. Li, M. Y. Xie, Z. Y. Ouyang, M. H. Xian, G. F. Huang, H. Wan, W. Hu and W. Q. Huang, *Adv. Energy Mater.*, 2024, **15**, 2404246.
22. W. Bao, J. Liu, T. Ai, J. Han, J. Hou, W. Li, X. Wei, X. Zou, Z. Deng and J. Zhang, *Adv. Funct. Mater.*, 2024, **34**, 2408364.
23. Y. Duan, Z. Y. Yu, S. J. Hu, X. S. Zheng, C. T. Zhang, H. H. Ding, B. C. Hu, Q. Q. Fu, Z. L. Yu, X. Zheng, J. F. Zhu, M. R. Gao and S. H. Yu, *Angew. Chem. Int. Ed.*, 2019, **58**, 15772-15777.
24. J. Sun, S. Zhou, Z. Zhao, S. Qin, X. Meng, C.-H. Tung and L.-Z. Wu, *Energy Environ. Sci.*, 2025, **18**, 1952-1962.
25. Q. Fu, L. W. Wong, F. Zheng, X. Zheng, C. S. Tsang, K. H. Lai, W. Shen, T. H. Ly, Q. Deng and J. Zhao, *Nat. Commun.*, 2023, **14**, 6462.
26. X. Ding, D. Liu, P. Zhao, X. Chen, H. Wang, F. E. Oropeza, G. Gorni, M. Barawi, M. García-Tecedor, V. A. de la Peña O'Shea, J. P. Hofmann, J. Li, J. Kim, S. Cho, R. Wu and K. H. L. Zhang, *Nat. Commun.*, 2024, **15**, 5336.
27. Y. Yao, G. Zhao, X. Guo, P. Xiong, Z. Xu, L. Zhang, C. Chen, C. Xu, T.-S. Wu, Y.-L. Soo, Z. Cui, M. M.-J. Li and Y. Zhu, *J. Am. Chem. Soc.*, 2024, **146**, 15219-15229.
28. J. Sang, P. Wei, T. Liu, H. Lv, X. Ni, D. Gao, J. Zhang, H. Li, Y. Zang, F. Yang, Z. Liu, G. Wang and X. Bao, *Angew. Chem. Int. Ed.*, 2021, **61**, e202114238.
29. P. Tian, W. Zong, J. Xiong, W. Liu, J. Liu, Y. Dai, J. Zhu, S. Huang, S. Song, K. Chu, G. He and N. Han, *Adv. Funct. Mater.*, 2025, **5**, 2504862.
30. J. Feng, X. Wang and H. Pan, *Adv. Mater.*, 2024, **36**, 2411688.
31. B. Lu, C. Wahl, R. dos Reis, J. Edgington, X. K. Lu, R. Li, M. E. Sweers, B. Ruggiero, G. T. K. K. Gunasooriya, V. Dravid and L. C. Seitz, *Nat. Catal.*, 2024, **7**, 868-877.
32. L. Wang, Y. Hao, L. Deng, F. Hu, S. Zhao, L. Li and S. Peng, *Nat. Commun.*, 2022, **13**, 5785.
33. J. T. Mefford, A. R. Akbashev, M. Kang, C. L. Bentley, W. E. Gent, H. D. Deng, D. H. Alsem, Y.-S. Yu, N. J. Salmon, D. A. Shapiro, P. R. Unwin and W. C. Chueh, *Nature*, 2021, **593**, 67-73.
34. J.-W. Zhao, H.-Y. Wang, L. Feng, J.-Z. Zhu, J.-X. Liu and W.-X. Li, *Chem. Rev.*, 2023, **124**, 164-209.
35. J. Zhou, J. Lin, X. Huang, Y. Zhou, Y. Chen, J. Xia, H. Wang, Y. Xie, H. Yu, J. Lei, D. Wu, F. Liu, Q. Fu, Q. Zeng, C.-H. Hsu, C. Yang, L. Lu, T. Yu, Z. Shen, H. Lin, B. I. Yakobson, Q. Liu, K. Suenaga, G. Liu and Z. Liu, *Nature*, 2018, **556**, 355-359.
36. W. Zhai, J. Qi, C. Xu, B. Chen, Z. Li, Y. Wang, L. Zhai, Y. Yao, S. Li, Q. Zhang, Y. Ge, B. Chi, Y. Ren, Z. Huang, Z. Lai, L. Gu, Y. Zhu, Q. He and H. Zhang, *J. Am. Chem. Soc.*, 2023, **145**, 13444-13451.
37. Z. Li, L. Zhai, Q. Zhang, W. Zhai, P. Li, B. Chen, C. Chen, Y. Yao, Y. Ge, H. Yang, P. Qiao, J. Kang, Z. Shi, A. Zhang, H. Wang, J. Liang, J. Liu, Z. Guan, L. Liao, V. A. Neacșu, C. Ma, Y. Chen, Y. Zhu, C.-S. Lee, L. Ma, Y. Du, L. Gu, J.-F. Li, Z.-Q.

View Article Online
DOI: 10.1039/D6EY00096G

Tian, F. Ding and H. Zhang, *Nat. Mater.*, 2024, **23**, 1355-1362.

38. Q. Gao, H. Chen, W.-s. Lu, Y.-h. Chan, Z. Chen, Y. Huang, Z. Liu and P. Chen, *Nat. Commun.*, 2025, **16**, 3784.
39. Z. Lai, Q. He, T. H. Tran, D. V. M. Repaka, D.-D. Zhou, Y. Sun, S. Xi, Y. Li, A. Chaturvedi, C. Tan, B. Chen, G.-H. Nam, B. Li, C. Ling, W. Zhai, Z. Shi, D. Hu, V. Sharma, Z. Hu, Y. Chen, Z. Zhang, Y. Yu, X. Renshaw Wang, R. V. Ramanujan, Y. Ma, K. Hippalgaonkar and H. Zhang, *Nat. Mater.*, 2021, **20**, 1113-1120.
40. R. Yang, L. Mei, Q. Zhang, Y. Fan, H. S. Shin, D. Voiry and Z. Zeng, *Nat. Protoc.*, 2022, **17**, 358-377.
41. R. Yang, L. Mei, Z. Lin, Y. Fan, J. Lim, J. Guo, Y. Liu, H. S. Shin, D. Voiry, Q. Lu, J. Li and Z. Zeng, *Nat. Rev. Chem.*, 2024, **8**, 410-432.
42. A. Han, X. Zhou, X. Wang, S. Liu, Q. Xiong, Q. Zhang, L. Gu, Z. Zhuang, W. Zhang, F. Li, D. Wang, L.-J. Li and Y. Li, *Nat. Commun.*, 2021, **12**, 709.
43. L. Xie, L. Wang, X. Liu, J. Chen, X. Wen, W. Zhao, S. Liu and Q. Zhao, *Nat. Commun.*, 2024, **15**, 5702.
44. B. Zhou, J. Zhou, L. Wang, J. H. Kang, A. Zhang, J. Zhou, D. Zhang, D. Xu, B. Hu, S. Deng, L. Huang, C. W. Wong, Y. Huang and X. Duan, *Nat. Synth.*, 2023, **3**, 67-75.
45. J. Wu, Z. Chen, K. Yang, X. Zhou, H. Li, Z. Wang, M. Su, R. Zhang, T. Wang, Q. Hu, N. Yan, C. Liu, B. Zhang, M. Yang, S. Xi and K. P. Loh, *Nat. Nanotechnol.* 2025, **20**, 1043-1051.
46. L. Mei, Z. Gao, R. Yang, Z. Zhang, M. Sun, X. Liang, Y. Zhang, T. Ying, H. Hu, D. Li, Q. Zhang, M. D. Gu, L. Gu, J. Zhou, B. Huang, D. Voiry, X. C. Zeng, Y. Chai, J. Li, X. Yu and Z. Zeng, *Nat. Synth.,* 2024, **4**, 303-313.
47. T. Gao, J. Gu, C. Yang, R. Wang, C. Wang, P. Zhang, J. Li, X. Zheng, Y. Fan, P. Yang, X. Hua, J. Hui and H. Zhang, *J. Am. Chem. Soc.*, 2025, **147**, 25385-25396.
48. W. Hou, A. Azizimanesh, A. Dey, Y. Yang, W. Wang, C. Shao, H. Wu, H. Askari, S. Singh and S. M. Wu, *Nat. Electron.*, 2023, **7**, 8-16.
49. Y. Sun, Y. Zang, W. Tian, X. Yu, J. Qi, L. Chen, X. Liu and H. Qiu, *Energy Environ. Sci.*, 2022, **15**, 1201-1210.
50. Y. He, L. Liu, C. Zhu, S. Guo, P. Golani, B. Koo, P. Tang, Z. Zhao, M. Xu, C. Zhu, P. Yu, X. Zhou, C. Gao, X. Wang, Z. Shi, L. Zheng, J. Yang, B. Shin, J. Arbiol, H. Duan, Y. Du, M. Heggen, R. E. Dunin-Borkowski, W. Guo, Q. J. Wang, Z. Zhang and Z. Liu, *Nat. Catal.*, 2022, **5**, 212-221.
51. X. Wang, B. Liu, S. Ma, Y. Zhang, L. Wang, G. Zhu, W. Huang and S. Wang, *Nat. Commun.*, 2024, **15**, 2600.
52. Z. Shi, W. Qin, Z. Hu, M. Ma, H. Liu, Z. Shu, Y. Jiang, H. Xia, W. Shi, C. Y. Zhang, X. Sang, C. Guo, Y. Li, C. Liu, C. Gong, H. Wang, S. Liu, L. Tapasztó, C. Gao, F. Liu, P. Tang, Y. Liu, H. Duan, E. Xie, Z. Zhang, Z. Liu and Y. He, *Nat. Mater.*, 2025, **24**, 1186-1194.
53. J. Wang, Y. Sun, Y. Cui and H. Qiu, *Energy Environ. Sci.*, 2025, **18**, 1756-1766.
54. Y. Kang, S. Li, O. Cretu, K. Kimoto, Y. Zhao, L. Zhu, X. Wei, L. Fu, D. Jiang, C. Wan, B. Jiang, T. Asahi, D. Zhang, H. Li and Y. Yamauchi, *Sci. Adv.*, 2024, **10**, eado2442.
55. B. Wu, X. Liu, P. Liu, G. Wu, L. Tian, X. Han, J. Li and X. Hong, *Nat. Synth.*, 2025, **4**, 370-379.
57. Z. Li, H. Yang, M. Sun, A. Zhang, Y. Ge, X. Long, B. Huang, L. Zhai, W. Zhai, L. Li, L. Wang, C. Wang, Y. Xu, Y. Cai, P. Liu, B. Chen, L. Gu, P. Qiao, Q. Zhang, F. Ding and H. Zhang, *J. Am. Chem. Soc.*, 2026, **148**, 7342-7354.
58. S. Zha, C. Lin and T. S. Choksi, *ACS Catal.*, 2026, **16**, 6098-6121.
59. A. Das, B. K. Das and K. K. Chattopadhyay, *Comput. Mater. Sci.*, 2023, **229**, 112418.

View Article Online
DOI: 10.1039/D6EY00096G

Data Availability Statement

The data supporting this article have been included as part of the Supplementary Information.